Available online at www.sciencedirect.com
ScienceDirect
International Journal of Heat and Mass Transfer 51 (2008) 1349–1364
International Journal of HEAT and MASS TRANSFER
www.elsevier.com/locate/ijhmt

Flow boiling of water in a circular staggered micro-pin fin heat sink

Santosh Krishnamurthy, Yoav Peles *

Department of Mechanical, Aerospace, and Nuclear Engineering, Rensselaer Polytechnic Institute, Troy, NY 12180, USA

Received 3 September 2007
Available online 10 January 2008

Abstract

Flow boiling of water across a bank of circular staggered micro-pin fins, 250 μm long and 100 μm diameter with pitch-to-diameter ratio of 1.5, was experimentally studied for mass fluxes ranging from 346 kg/m^2 s to 794 kg/m^2 s and surface heat fluxes ranging from 20 W/cm^2 to 350 W/cm^2. Local temperature measurements were used to elucidate the two-phase heat transfer coefficients. The flow was visualized and classified as vapor slug and annular flow patterns. A flow map was constructed and compared with maps for adiabatic micro-scale systems and good agreement was observed. A superposition model for the two-phase heat transfer coefficient in convective boiling regime was developed. Frictional multiplier, $((\phi_l)^2)$, from micro-scale studies was used to define the enhancement factor (F) in the heat transfer coefficient model and reasonable agreement was obtained between experiments and predictions.

Keywords: Pin fins; Micro-scale; Heat transfer coefficient; Boiling; Flow patterns

1. Introduction

Single-phase [1–5] and two-phase flows [6–9] in micro-channel heat sinks have been extensively studied and developed over the last several years in pursuit of cooling method for ultra high power electronic systems. Recently, configurations like pin fin based micro-channel heat sinks have also been explored, but primarily for single-phase flow [10–14].

The interdependency of the hydraulic and thermal processes of two-phase flow has resulted in two separate type of studies: adiabatic [15–18] and diabatic [19–23]. Adiabatic flow studies are generally tailored to identify the flow patterns and to develop prediction methods for the two-phase frictional multiplier and the void fraction. Diabatic studies mainly focus on investigating the two-phase heat transfer coefficients, the onset of nucleate boiling, and the critical heat flux (CHF). For example, under adiabatic flow conditions, Grant and Chislom [24] identified four different flow patterns: bubbly, spray, stratified-spray, and stratified flows. Schrage and Jensen [18] developed a correlation for the two-phase frictional multiplier based on these flow patterns and reported good agreement with their experimental results. For diabatic flow, Jensen and Hsu [21], in their parametric study on two-phase flow across a bank of heated tube bundles, have shown that the local two-phase heat transfer coefficient is a function of both mass flux and heat flux. They later used the correlation suggested by Schrage and Jensen [18] for the two-phase frictional multiplier to predict the two-phase heat transfer coefficient using Chen-type [20] correlation. Similarly, Polley et al. [23] developed a correlation for the void fraction, which was later used by Hwang and Yao [22] to calculate the enhancement factor (F) and to predict the two-phase heat transfer coefficients. Dowlati et al. [25] conducted boiling experiments using R-113 across a tube bundle and determined the void fraction, the frictional pressure drop, and the local heat transfer coefficients. They correlated their experimental data using pool boiling correlation and concluded that nucleate boiling is the dominant heat transfer mechanism in the range of heat flux they studied.

Previous efforts on adiabatic [26–29] and diabatic [6,7,30] two-phase flow at the micro-scale mainly concerned flow in

* Corresponding author.
E-mail address: pelesy@rpi.edu (Y. Peles).

0017-9310/$ - see front matter © 2007 Elsevier Ltd. All rights reserved.
doi:10.1016/j.ijheatmasstransfer.2007.11.026

Nomenclature

A_p	planform area, m^2
$A_{c,fin}$	cross-sectional area of the pin fin, m^2
C_p	specific heat, kJ/(kg °C)
C	constant in Eq. (45)
C_1	constant in Eq. (44)
d	pin fin diameter
F	enhancement factor
f	friction factor
G	mass flux, kg/(m^2 s)
H	height of the device, m
$\bar{h}_{avg}$	average heat transfer coefficient, W/(m^2 °C)
$\bar{h}_x$	local heat transfer coefficient, W/(m^2 °C)
h	heat transfer coefficient, W/(m^2 °C)
I	current, A
j_l	superficial liquid velocity, m/s
j_g	superficial gas velocity, m/s
k_s	thermal conductivity of silicon, W/(m °C)
L	length of the device, m
MAE	mean average error
N_{row}	number of pin fin rows in longitudinal direction
N_t	total number of pin fins
$\overline{Nu}_{avg}$	average Nusselt number
$\overline{Nu}_x$	local Nusselt number
Pr_s	Prandtl number at the surface
P_{fin}	perimeter of a fin, m
ΔP_{meas}	measured pressure drop, kPa
ΔP_{or}	pressure drop across orifice, kPa
ΔP_{fin}	Pressure drop across pin fins, kPa
Re	Reynolds number
P	power, W
Q_{loss}	heat loss, W
q''	heat flux, W/m^2
R	resistance, Ω
Re	Reynolds number, $Re = Gd/\mu$
S	suppression factor
$\overline{T}_{surface}$	surface temperature, °C
$\overline{T}_{heater}$	temperature of the heater, °C
T_{mi}	mean fluid temperature at the inlet, °C
T_{me}	mean fluid temperature at the exit, °C
$T_{s,x}$	local surface temperature, °C
T_{sat}	saturation liquid temperature, °C
t	thickness of the device, m
V	voltage, V
v	velocity, m/s
w	width of the device, m
X	Martinelli parameter

Greek symbols

ρ	density, kg/m^3
η_f	fin efficiency
ϕ_l	liquid two-phase frictional multiplier
τ	shear stress, N/m^2
μ	viscosity, kg/(m s)
ζ	adjustment parameter

Subscripts

f	fluid
tp	two-phase
sp	single-phase
d	pin fin diameter
nb	nucleate boiling
cv	convective
tt	turbulent–turbulent
vv	viscous–viscous
w	wall
l	liquid
g	gas

straight wall microchannels, but very limited studies have been performed on flow across micro-pin fins. Recently, Koşar and Peles [31] reported flow boiling across a bank of hydrofoil pin fins using R-123. They observed nucleate boiling at low heat fluxes and convective boiling at high heat fluxes. They further developed a correlation to predict the heat transfer coefficients using Chen-type correlation and identified bubbly, intermittent, and spray flow patterns. Their experiments were conducted at high mass fluxes to avoid flow instabilities. Krishnamurthy and Peles [32] conducted adiabatic water-nitrogen experiments on flow across a bank of micro-pillars and identified four flow patterns: bubbly-slug, gas-slug, bridge, and annular. They further developed a correlation for two-phase frictional multiplier as a function of mass flux and flow patterns.

Studies on flow boiling at the micro-scale suggest that heat transfer and fluid flow at diminishing length scale have some unique characteristics. Rapid bubble growth [33–35], different dependency, than in conventional scale, of the heat transfer coefficient on heat flux [9,31,36,37], mass flux, and quality [7,9], increased heat flux at the onset of nucleate boiling [7], and length scale dependency of the two-phase frictional multiplier [26,29,32,38,39] are all characteristics of the micro-scale. With the existing limited experimental evidence, it is not prudent to employ large scale knowledge and correlation to predict the corresponding physical phenomena, such as the heat transfer coefficient, pressure drop, and flow patterns, for other 'non-conventional' microchannels flow configuration. Furthermore, even at the macro-scale, it is commonly accepted that no general applicable correlation is available that is capable of predicting heat transfer coefficient over a large range of forced convection thermal-hydraulic conditions and tube bundle/pin-fin configurations [17,21,40]. A parametric study of the effect of surface tension and flow configurations on cross flow boiling in micro-scale still needs to be undertaken.

This report presents results on crossflow boiling in circular staggered micro-pin fin heat sink using water. The device used in the current investigation features an array of inlet orifices to avoid flow instabilities [41] and thermistors at three locations along the channel length for local temperature measurements. A new correlation along the lines of Chen [20] and Bennett and Chen [19] models, has been developed to predict the two-phase heat transfer coefficient for flow across micro-pin fins. Section 2 provides a detailed overview of the device geometry and presents the essential micro-fabrication process flow used. Additionally, an overview of the experimental apparatus and procedure is presented. Section 3 presents the methodology used to reduce the data. Section 4 includes discussion on flow patterns and heat transfer mechanisms, experimental results on single-phase and two-phase heat transfer coefficients, and the development of the new correlation.

2. Device overview, fabrication and experimental procedure

The following section provides a detailed overview of the device and the micro-fabrication process flow used to micro-fabricate the devices.

2.1. Device overview

A computer aided design (CAD) schematic of the device consisting of a 1800 μm wide and 1 cm long microchannel of depth 250 μm is shown in Fig. 1. The microchannel encompass 68 rows of 11 and 12 (in tandem) staggered circular 100 μm diameter pin fins. Pressure taps are placed at the inlet and exit to enable pressure measurements. Upstream the main pin fin array, five micro-orifices, each 400 μm long with 20 μm opening, are placed. A heater is deposited on the backside of the device, under the pin fin array. Prior to the heater deposition, three thermistors, along with their respective thermal vias for outer electrical connections, are deposited on the backside of the wafer. The thermistors are located at the entrance, 3.33 mm, and 6.67 mm downstream the first row of pin fins and are expressed as T_1, T_2, and T_3, respectively. A Pyrex cover seals the device from the top and allows flow visualization.

2.2. Micro-fabrication process flow

A double side polished, n-type ⟨100⟩ single crystal silicon wafer was processed on both sides to create the MEMS device, which consists of a microchannel enclosing an array of pin fins. In the fabrication process first, the top side and bottom side masks were designed and fabricated. A 1 μm thick thermal oxide was grown on both sides of the silicon wafer to protect the bare wafer surface. A 100 Å thick layer of titanium was deposited on the back side of the wafer using cryopumped CVC 601 sputter deposition system. This was followed by a photolithography and wet bench process to form thermistors used for local temperature measurements. Thermal vias were later formed by depositing 0.2 μm thick layer of aluminum containing 1% silicon and 4% copper in a CVC sputter system followed by subsequent photolithography and wet bench process. A 1 μm

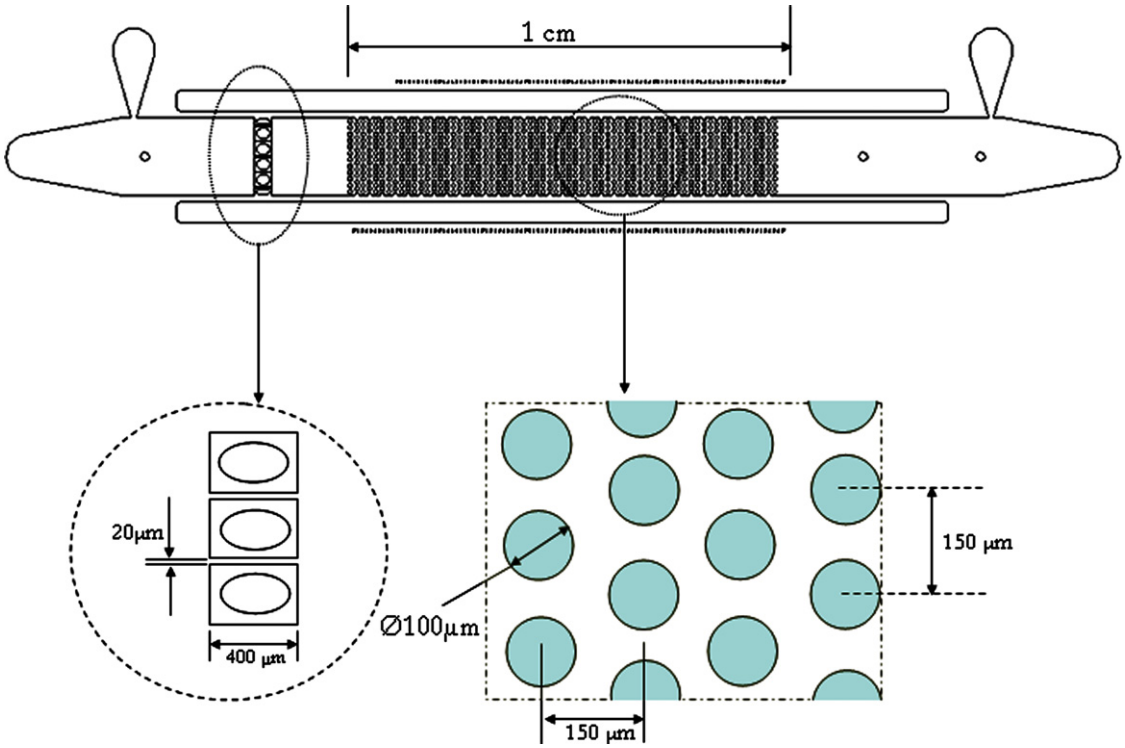

Fig. 1. Device overview of the dimensions of inlet orifice and pin fin section.

thick thermal oxide was then deposited on the newly formed thermistors and vias using GSI-PECVD system. The heaters and vias were deposited on the back side of the wafer by a CVC deposition system. A 70 Å thick layer of titanium was initially deposited to enhance adhesion and was followed by sputtering a 1 μm thick layer of aluminum containing 1% silicon and 4% copper. Subsequent photolithography and concomitant wet bench processing created the heater on the back side of the wafer. Next, the microchannel with the micro-pin fins was formed on the top side of the wafer. For this, the wafer was taken through a photolithography step and a reactive ion etching (RIE) oxide removal process to mask certain areas on the wafer, which were not to be etched during the deep reactive ion etching (DRIE) process. The wafer was consequently etched in a DRIE process, and silicon was removed from places not protected by the photoresist/oxide mask. The DRIE process formed deep vertical trenches on the silicon wafer with a characteristic scalloped sidewall possessing a peak-to-peak roughness of 0.3 μm. A profilometer and an SEM were employed to measure and record various dimensions of the device. The wafer was flipped and the back side was then processed, so that an inlet, exit, side air gap, and pressure port taps for the transducers were formed. Photolithography followed by a buffered oxide etch (BOE) (6:1) oxide removal process was carried out to create a pattern mask. The wafer was then etched-through in a DRIE process to create the fluidic ports. Thereafter, electrical con-

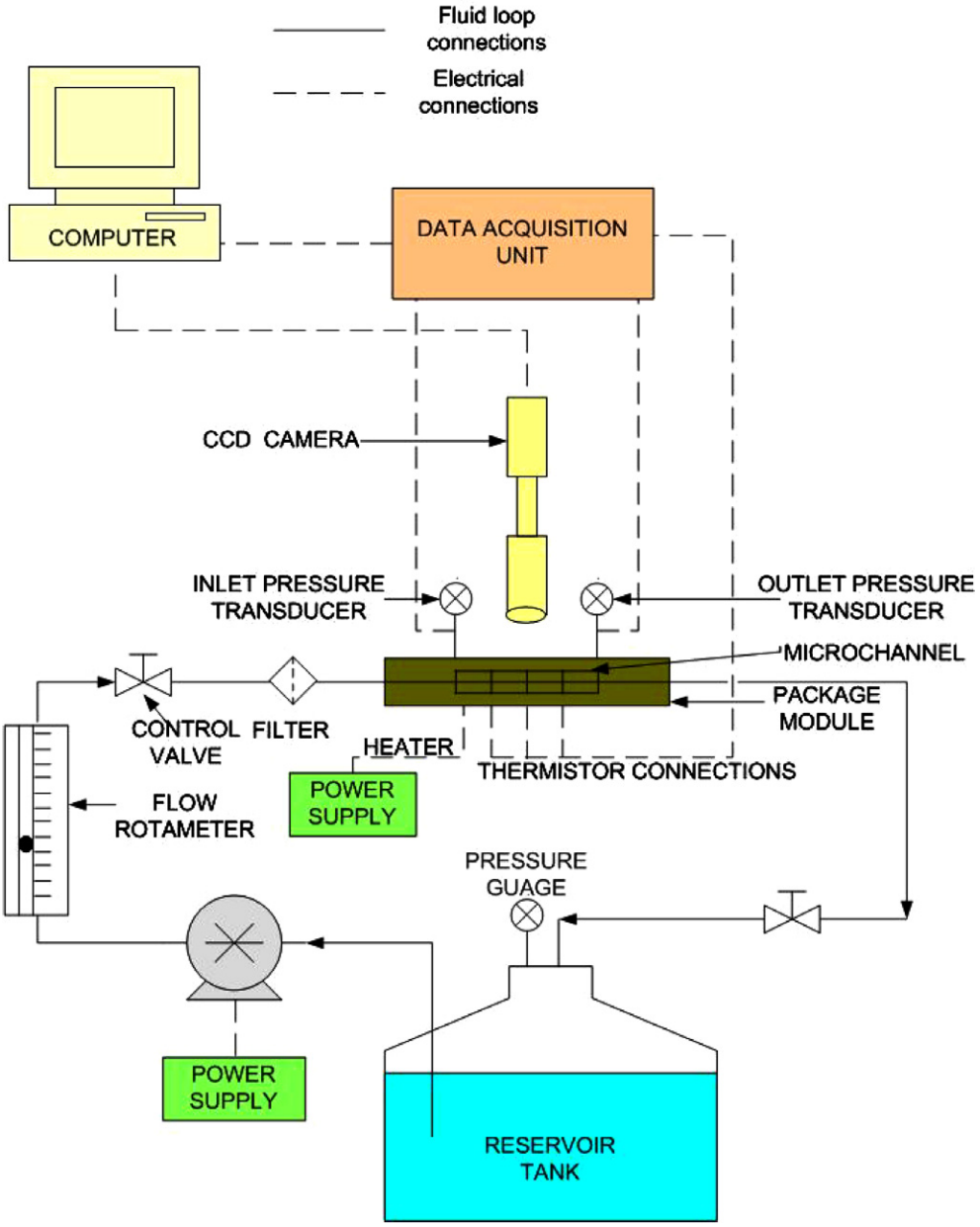

Fig. 2. Schematic of the experimental set up.

tacts/pads were opened on the back side of the wafer by performing another round of photolithography and RIE processing. Finally, the processed wafer was stripped of any remaining resist or oxide layers and anodically bonded to a 1 mm thick polished Pyrex™ (glass) wafer to form a sealed device. After the completion of the bonding process, the wafer is visually inspected for any fringes or voids which are indicative of an ineffective bonding. In case, if any fringes are found on the wafer, the wafer stack is again taken through a bonding process in an attempt to remove these defects. After successful completion of the bonding process, the processed stack was die-sawed to separate the devices from the parent wafer.

2.3. Experimental apparatus and procedure

The schematic of the experimental set up used is shown in Fig. 2. The major components of the set up include a pump, a flow meter, filters, a packaging module and the micro-pin fin device. The MEMS device was sandwiched between an upper plate and the package module through a series of o-rings, which act as hermetic seals and connect the pressure ports and inlet/outlet of the channel to the flow loop, as shown in Fig. 3. External electrical connections for the heater and the thermistors were made from the bottom by means of spring loaded pins, which connect the heater and the thermistors to electric pads residing away from the main pin fin body device. Resistance, pressure, and flow measurements were taken at a fixed flow rates in the loop. The electric power to the heater was supplied with an INSTEK programmable power supply, while electrical current and voltage were measured through HP digital multimeter. The liquid was propelled through a reservoir by means of a HNP Mikrosysteme micro-annular gear pump, which is capable of generating flow rates from 0.3 to 18 ml/min. The pressure ports were connected to pressure transducers (Omega Engineering, Inc.), each capable of measuring pressures of up to 200 psia via the packaging module. The water flow meter (Omega Engineering, Inc, FL-111 series) is capable of reading flow rates from 0.138 to 16.38 ml/min. The flow rate, current, and voltage data are manually collected, while the data from the pressure transducer and thermistors were delivered to the PC based LabVIEW® program and stored in a file for further analysis. The flow was proctored with a microscope and flow images were taken via a Vision Research Phantom V-4 series high-speed camera capable of capturing frames with a rate up to 90,000 frames per second, a maximum resolution of 512 × 512 pixels, and a minimum exposure time of 2 μs.

In the experimental procedure, the heater and the thermistors were first calibrated in a well insulated oven to obtain resistance–temperature calibration curves. The calibration curves obtained for the heaters and thermistors are shown in Fig. 4. These curves were later used for data reduction process to obtain the mean surface and local temperatures. A standard deviation of 0.15 °C was obtained between the individual data points and the calibration curve. This was followed by placing the device in the module package, which was connected to the flow loop.

In order to estimate the heat losses, the electrical power was applied to the test section before flooding the device with the liquid. Once the temperature of the test section reached steady state condition, the temperature difference between the ambient and the test section and the corresponding power were recorded. The temperature difference–power

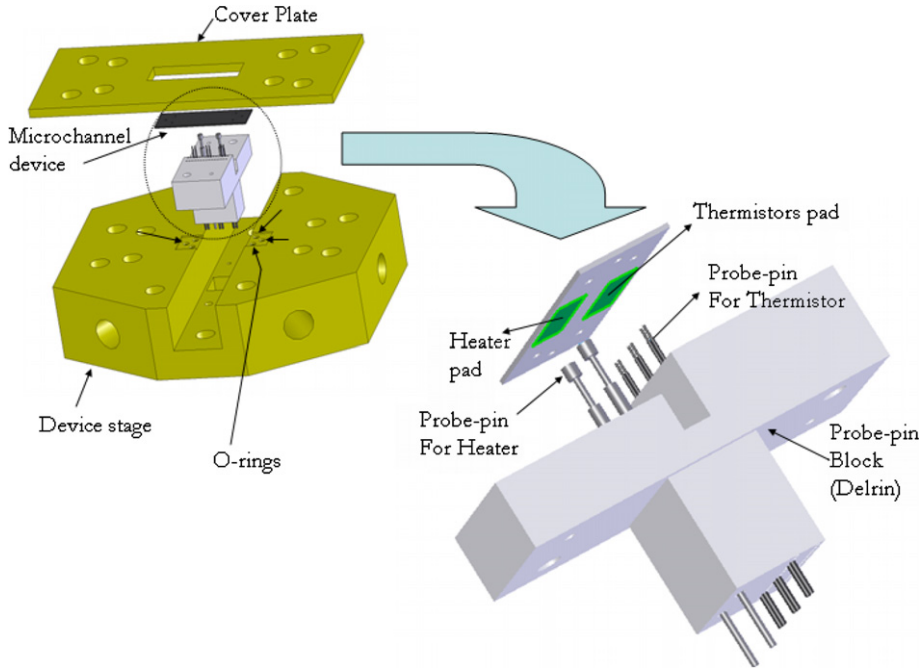

Fig. 3. Package module for the device.

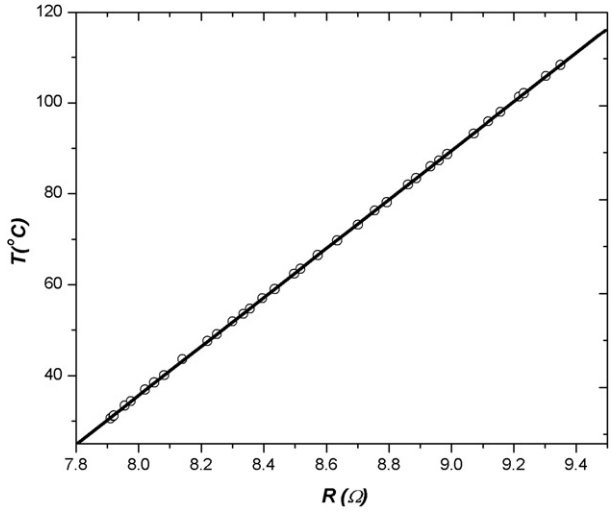

(a) Heater

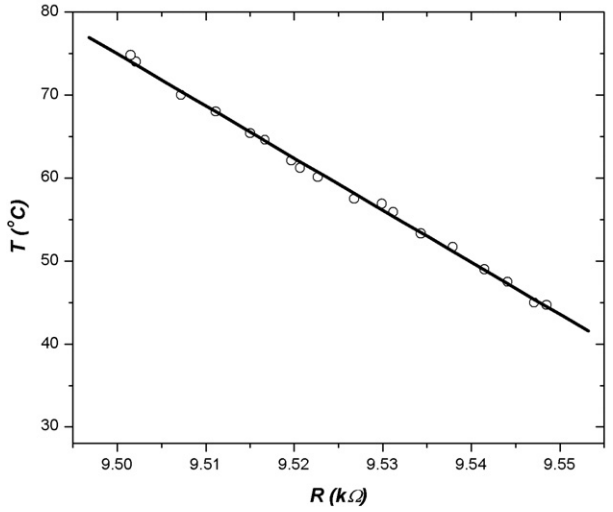

(b) Thermistor

Fig. 4. Calibration curves.

curve was used to estimate the heat loss for every datum point. The measured heat loss was then subtracted from the total supplied power to the heat sink, and the corresponding values were used in the data reduction analysis. The measured heat losses for the current experiment were found to be less than 7% for all the experimental conditions. The flow rate was fixed at a desired value, and the data were taken after steady state flow conditions were reached. The exit pressure of the channel was maintained at atmospheric pressure (101.325 kPa). Before the data acquisition process, the electrical resistances of the heater and thermistors were measured at room temperature. To obtain the heat transfer data, the voltage across the resistance was increased in steps of 0.5 V, and the current/voltage data were recorded while ensuring constant flow rate. Simultaneously, the resistance from the thermistors were recorded through the LabVIEW® interface in a spreadsheet. The voltage was monotonically increased, until a surge in the resistance corresponding to increase in temperature (i.e., CHF conditions) of the device was detected. The power was switched off in order to secure the device. The procedure was followed for all flow rates.

3. Data reduction

The voltage, current and pressure measurements were used to obtain the single-phase and two-phase pressure drops and heat transfer coefficients. The following section gives the data reduction procedure used to obtain these parameters.

3.1. Single-phase heat transfer

The voltage and current values were used to calculate the input power and heater resistance:

$$P = VI, \tag{1}$$

$$R = V/I. \tag{2}$$

The average heater temperature and the local temperatures from the thermistors were obtained from the calibration curve shown in Fig. 4. Assuming 1D steady state conduction through the silicon block, the average surface temperature of the device was obtained by:

$$\overline{T}_{\text{surface}} = \overline{T}_{\text{heater}} - \frac{(P - Q_{\text{loss}})t}{k_s A_p}. \tag{3}$$

The local surface temperatures obtained from the resistances of the individual thermistors were also derived in a similar method. The average heat transfer coefficient was obtained using Newton's law of cooling jointly with 1D steady state adiabatic fin tip equation:

$$(P - Q_{\text{loss}}) = \bar{h}_{\text{avg}}(\eta_f N_t P_{\text{fin}} H + wL - N_t A_{c,\text{fin}}) \times \left(\overline{T}_{\text{heater}} - \frac{T_{\text{mi}} + T_{\text{me}}}{2}\right), \tag{4}$$

where $\eta_f = \frac{\tanh(mH)}{mH}$, $m = \sqrt{\frac{\bar{h}_{\text{avg}} P_{\text{fin}}}{k_s A_{c,\text{fin}}}}$, and $T_{\text{me}} = T_{\text{mi}} + \frac{(P - Q_{\text{loss}})}{\dot{m} C_p}$. The above equation was solved iteratively to obtain $\bar{h}_{\text{avg}}$. The local heat transfer coefficient was calculated according to:

$$(P - Q_{\text{loss}}) = h_x(\eta_f N_t P_{\text{fin}} H + wL - N_t A_{c,\text{fin}})(T_x - T_{mx}), \tag{5}$$

where $T_{mx} = T_{\text{mi}} + \left(\frac{(P - Q_{\text{loss}})}{\dot{m} C_p} \frac{L_x}{L}\right)$.

The statistical average value of the heat transfer coefficients $\overline{h_x}$, $\overline{h_{\text{avg}}}$ and the corresponding Nusselt numbers over all heat fluxes for a fixed Reynolds number are:

$$\overline{h_{\text{avg}}} = \frac{1}{M}\sum_{i=1}^{M} h_{\text{avg},i}, \tag{6}$$

$$\overline{h_x} = \frac{1}{M}\sum_{i=1}^{M} h_{x,i}, \tag{7}$$

$$\overline{Nu_{\text{avg}}} = \left(\frac{1}{M}\sum_{i=1}^{M} h_{\text{avg},i}\right)\frac{k_f}{d}, \tag{8}$$

$$\overline{Nu_x} = \left(\frac{1}{M}\sum_{i=1}^{M} h_{x,i}\right)\frac{k_f}{d}. \quad (9)$$

3.2. Two-phase heat transfer

The temperature obtained from the thermistor located downstream the inlet was used for all the two-phase heat transfer calculations. The local two-phase heat transfer coefficient was calculated as:

$$(P - Q_{loss}) = h_{tp}(\eta_f N_t P_{fin} H + wL - N_t A_{c,fin})(T_{s,x} - T_{sat}). \quad (10)$$

The saturation temperature at the location of the thermistor is a function of the local pressure. The local pressure in the two-phase regime is estimated by using a modified version of the Chisholm Correlation [15] for frictional multiplier $\left(\phi_l^2 = \frac{(\Delta P_f)_{tp}}{(\Delta P_f)_f}\right)$. Since the quality varies along the channel, the local two-phase pressure is calculated using the following expression:

$$\Delta P_{tp}(x) = \frac{1}{x - x_i}\int_{x_i}^{x} \phi_l^2 (\Delta P_f)_f \, dx + \Delta P_{accl} \quad (11)$$

No correlation for frictional multiplier is available for the current flow configuration and conventional scale correlations for similar configuration in micro-scale have been found to overpredict the experimental results [32]. Krishnamurthy and Peles [32] have shown that their experimental results were predicted with a MAE of 22.5% using the correlation developed by Kawahara et al. [29] for a 100 μm diameter micro-channel, given by:

$$\phi_l^2 = 1 + \frac{C}{X_{vv}} + \frac{1}{X_{vv}^2} \quad (12)$$

where $C = 0.24$ is an empirically defined constant. X_{vv} is the Martinelli parameter defined as:

$$X_{vv} = \left[\frac{(\Delta P_f/\Delta Z)_f}{(\Delta P_f/\Delta Z)_v}\right]^{\frac{1}{2}} \quad (13)$$

$$(\Delta P_f)_f = \frac{fN(G(1-x))^2}{2\rho_f} \quad (14)$$

$$(\Delta P_f)_v = \frac{fN(Gx)^2}{2\rho_v} \quad (15)$$

and f is the Blasius type friction factor, which was developed for a similar device by Koşar and Peles[10] and is defined as:

$$f = 63.246(Re_d)^{-0.7797} \quad (16)$$

where Re_d is the Reynolds number ($Re = Gd/\mu$). The above correlation was able to predict their experimental results within ±5%. Since the flow configuration used in the current study is similar, an uncertainty of 5% is associated with the friction factor. The acceleration pressure drop can be calculated as:

$$\Delta P_{accl} = \left\{\frac{G^2x^2}{\rho_g\alpha} + \frac{G^2(1-x)^2}{\rho_l(1-\alpha)}\right\}_{outlet} - \left\{\frac{G^2x^2}{\rho_g\alpha} + \frac{G^2(1-x)^2}{\rho_l(1-\alpha)}\right\}_{inlet}, \quad (17)$$

where α is void fraction, which is obtained by:

$$\frac{\alpha}{\alpha_h} = 1 + 0.04503(f)^{0.34}\ln(x) \quad (18)$$

α_h is the homogenous void fraction and f is the liquid friction factor. Based on the results of Krishnamurthy and Peles [32], an uncertainty of 20% is associated with the above correlation. Since the local quality is known, the local pressure can be estimated:

$$P_x = P_{exit} + \Delta P_{tp}(x). \quad (19)$$

The uncertainty associated with the resulting absolute local pressure was obatined by using propogation of uncertainty method and was found to be ±3%. This resulted in ±0.7 °C uncertainty in the saturation temperature. The saturation temperature corresponding to the local pressure was obtained from steam tables. The local saturation temperature at the third thermistor location (T_3), as a function of heat flux is shown in Fig. 5 for different mass fluxes. Comparison of the experimental data with existing models was done through the mean absolute error (MAE):

$$MAE = \frac{1}{M}\sum_{i=1}^{M}\frac{|\theta_{exp} - \theta_{pred}|}{\theta_{pred}} \times 100, \quad (20)$$

where θ is the measured physical quantity and the subscripts 'exp' and 'pred' refer to the experimental and predicted values, respectively. The uncertainty associated with the measured values were obtained from the manufacturers' specification sheets and is given in Table 1, while the uncertainty associated with the derived quantities was obtained by using the propagation of uncertainty analysis.

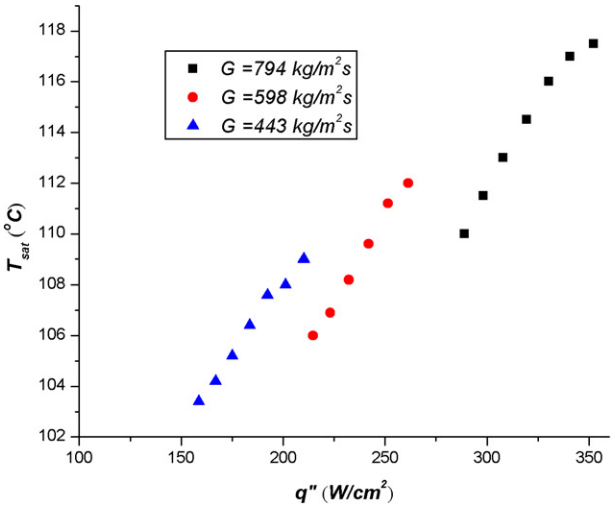

Fig. 5. Local saturation temperature as a function of heat flux.

Table 1
Uncertainty in variables

Uncertainty	Error
Flow rate, Q (for each reading) (%)	1
Voltage supplied by power source, V (%)	0.1
Current, I (%)	0.1
Tube hydraulic diameter, D (%)	1
Ambient temperature, T_{amb} (°C)	±1
Channel width, w (%)	1
Channel height, H (%)	0.67
Density of fluid, ρ_l (%)	0.5
Mass flux, G (%)	3.8
Local temperature, T_x (°C)	±0.5
Heat transfer coefficient, h_{tp} (%)	15–20

4. Results and discussion

The local surface temperature as a function of wall heat flux for different mass velocities is shown in Fig. 6. As expected, during single-phase flow, the temperature dependency on the heat flux is linear with decreasing slope for higher mass fluxes. At sufficiently high heat fluxes, boiling is triggered. The onset of boiling is clearly marked by a significant change in the $T - q''$ slope. Each curve, with the exception of $G = 794$ kg/m^2 s, can be divided into two regions of roughly constant slopes, corresponding to single-phase and fully developed boiling flow. For $G = 794$ kg/m^2 s, in addition to the above two distinct slopes, an intermittent slope corresponding to partial boiling region is apparent, but the transition from inception to fully developed boiling occurs over a limited range of heat fluxes.

The local single-phase heat transfer coefficient as a function of the wall heat flux for different mass fluxes is shown in Fig. 7a. The heat transfer coefficient increases with mass flux and is independent of wall heat flux. This is also characteristic of single-phase flow across pin fin systems in conventional scale and is in agreement with the single phase flow studies at the micro-scale [10]. It should be noted that the large heat transfer coefficients result in low surface-liquid temperature difference, which in turn increases the experimental measurement uncertainties. In Fig. 7b, the

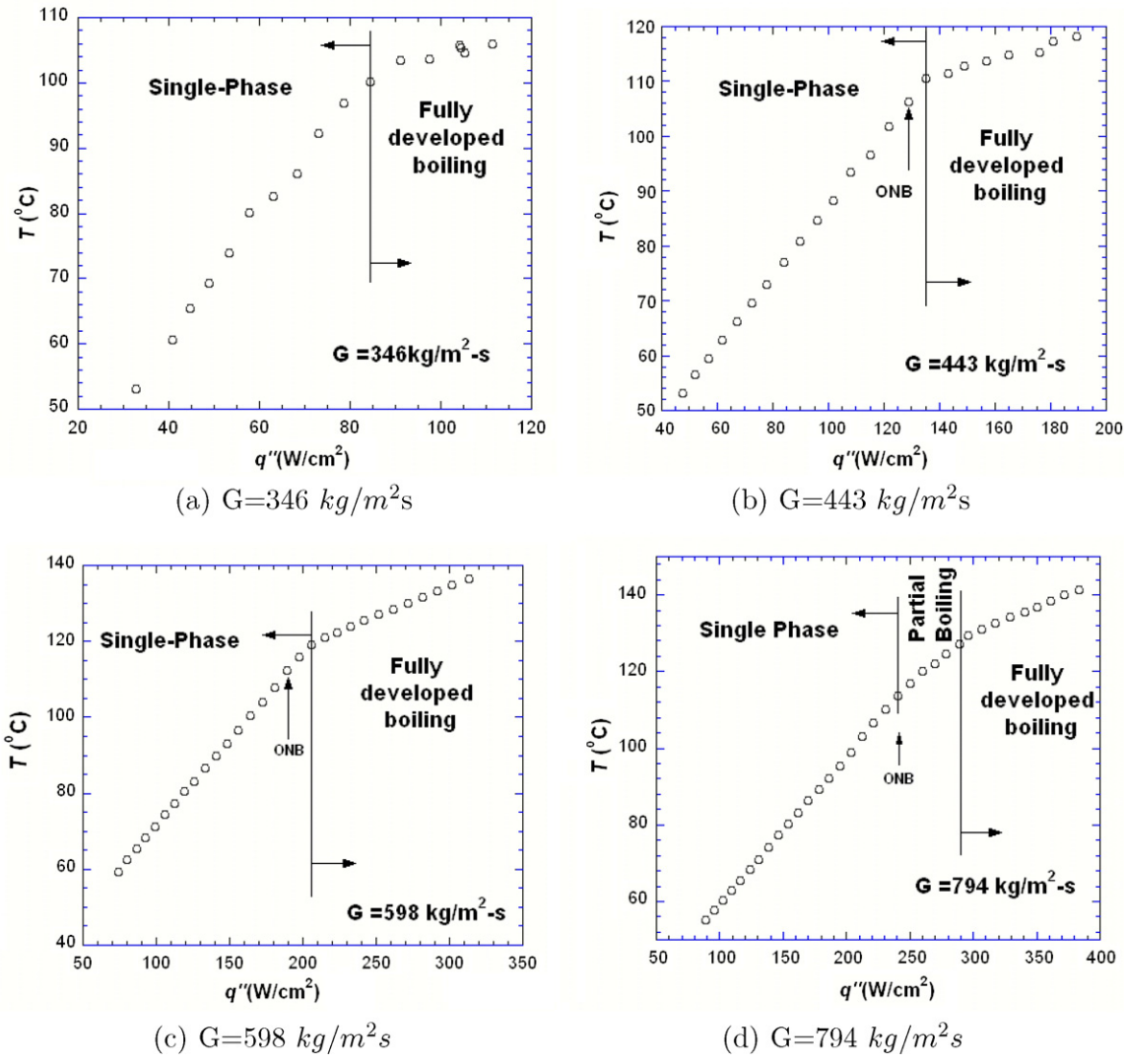

Fig. 6. Boiling curves for different mass fluxes.

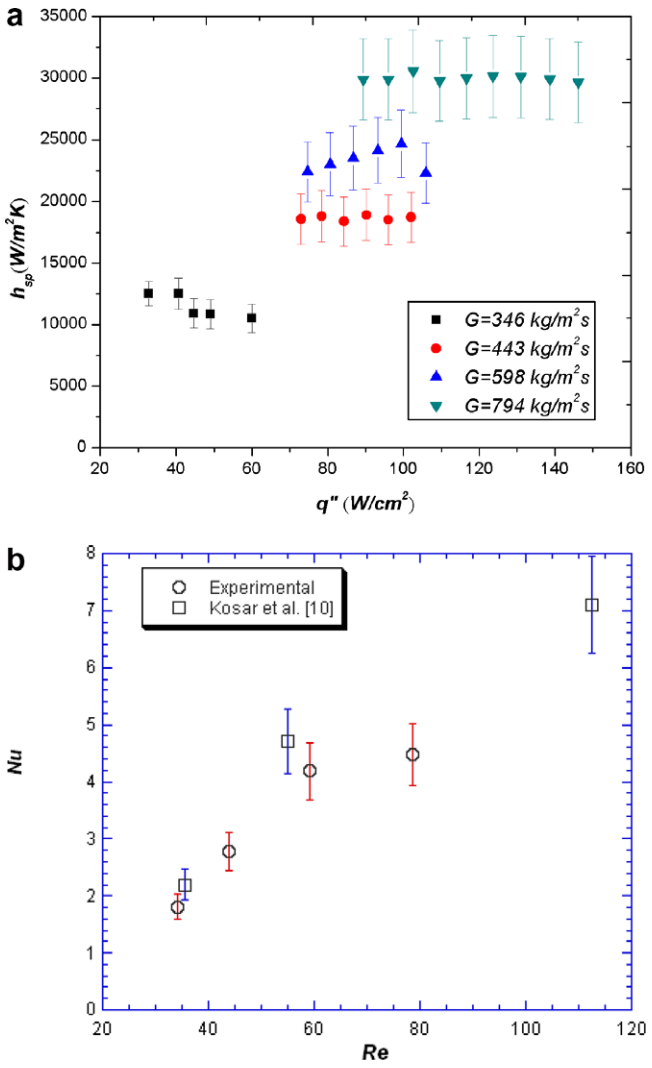

Fig. 7. (a) Single-phase heat transfer coefficient for different mass fluxes; (b) *Nu* vs. *Re*.

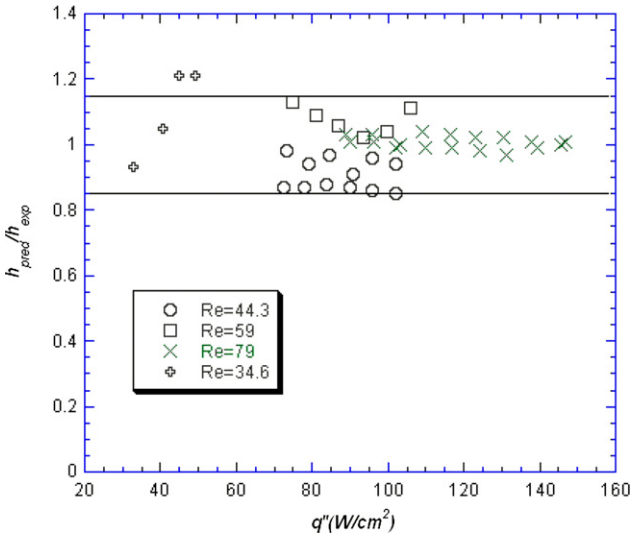

Fig. 8. Comparison between predicted and experimental values of single-phase heat transfer coefficient.

experimental Nusselt number as a function of the Reynolds number is compared with the results obtained by Koşar and Peles [10], and is found to be in good agreement. Fig. 8 compares the current local measurements with the Nusselt number correlation developed in [11]:

$$Nu_{sp} = 0.0423 Re_d^{0.99} Pr^{0.21} \left(\frac{Pr}{Pr_s}\right)^{0.25}. \quad (21)$$

Ninety five percent of the predicted data fall within ±15% of the experimental results. The mean average error (MAE) between the predicted and experimental results is 6.05%.

4.1. Two-phase flow patterns and heat transfer mechanisms

Flow boiling mechanisms vary for different flow patterns, e.g., bubbly flow is associated with nucleate boiling and annular flow pattern with convective film boiling [42]. For $G = 346$ kg/m^2 s, at heat fluxes slightly above the onset of boiling, vapor formed at nucleation sites in the vicinity of the channel exit. The hydraulic resistance imposed by the pin fins forced the bubbles to oscillate between the pin fins. The sliding motion of the bubble caused the thin liquid film between the surface and the bubble to evaporate and to form vapor cavity. High surface tension forces acting along the vapor–liquid interface, low superficial liquid velocity, and hydraulic resistance of the pin fins caused these vapor cavities to remain stationary (Fig. 9). With increasing heat flux, the vapor cavities grew, resulting in an increase in the local void fraction. This in turn increased the local superficial liquid velocity and, thus, the drag force on the vapor cavity forcing the bubbles to propagate downstream. At higher heat fluxes, annular flow was established.

For moderate mass fluxes ($G = 443$ kg/m^2 s, $G = 598$ kg/m^2 s), the bubbles generated at the nucleation site expanded and formed vapor slugs over a period of time, which ultimately departed and propagated downstream, as shown by the sequence of images in Fig. 10. The increased inertial and shear forces with increasing mass flux overcome the surface tension forces and promoted the detachment of the vapor slugs. At high heat flux, annular flow pattern was detected (Fig. 11).

For $G = 794$ kg/m^2 s, during partial boiling, the flow pattern was predominantly vapor slug. The slugs detached and propagated through the channel in quick succession. Unlike for low mass fluxes, the boiling front appeared to oscillate resulting in alternate zones of liquid and vapor. The effect of this phenomenon is vindicated by the presence of the intermediate slope region in the T vs. q'' curve (Fig. 6) corresponding to partial boiling. As the heat flux increased, these vapor slugs expanded triggering annular flow pattern.

The observed flow patterns are mapped as a function of the superficial vapor Reynolds number, Re_g, and liquid Reynolds number, Re_l, in Fig. 12 along the adiabatic flow

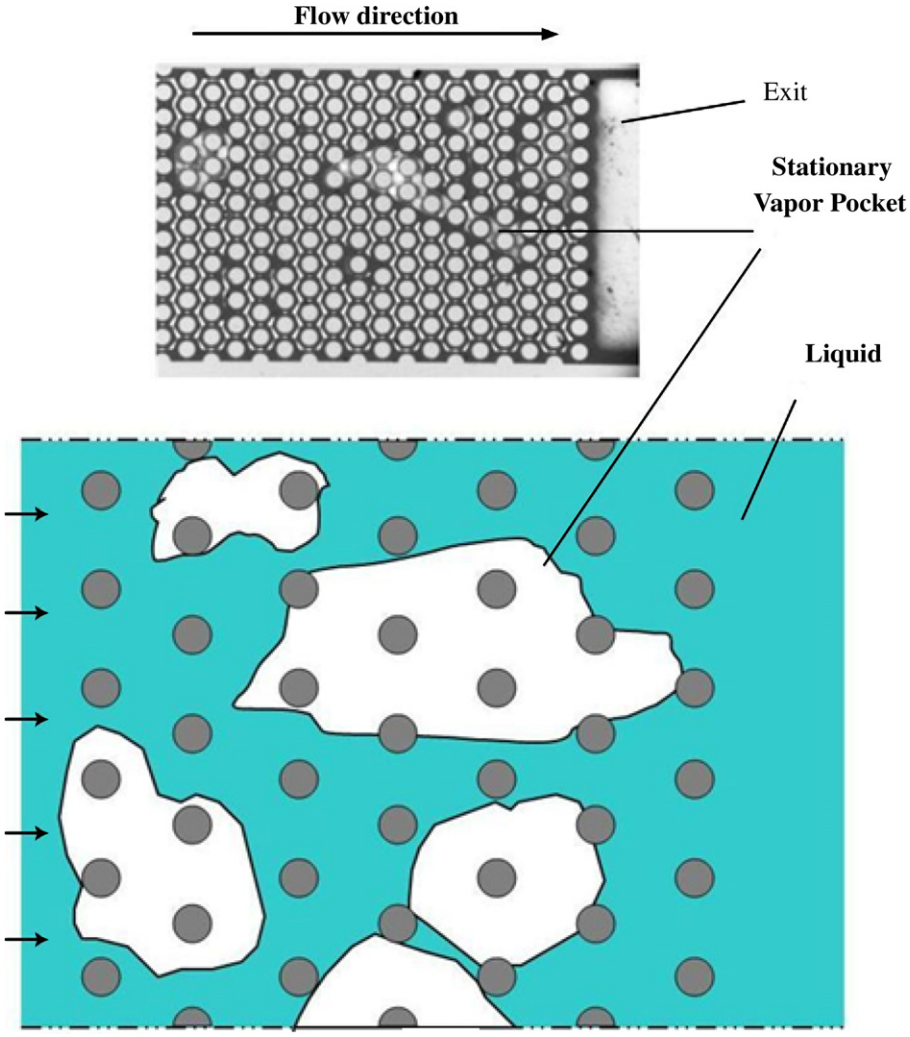

Fig. 9. Video image and schematic of stationary vapor pocket at $G = 346\ \mathrm{kg/m^2\ s}$.

map of Krishnamurthy and Peles [32] and Kawahara's et al. [29] 100 μm micro-channel. Generally the flow maps of the current study concur with other maps. Although bubble nucleation was observed, it appeared to be confined to a very limited region where the flow transitioned from single-phase to vapor–liquid two-phase flow-nucleation was generally suppressed. This is apparent by the persistence of the annular flow pattern over a wide range of heat and mass fluxes.

4.2. Heat transfer coefficients

Fig. 13 shows the local two-phase heat transfer coefficients as a function of the wall heat flux for various mass fluxes. As can be observed, the heat transfer coefficient moderately depends on the mass flux (Fig. 14) and is weakly dependent on the heat flux. This trend suggests that the dominant heat transfer mechanism is convective boiling, which is further supported by the presence of annular flow observed during flow visualization. While conventional scale studies suggest that the heat transfer coefficient depends on the mass flux, several micro-channel studies [9,36,43] argue that this is not a characteristic of the micro-scale. However, in the current study the heat transfer coefficient seems to be dependent on the mass flux.

4.3. Development of model

The contributions of the nucleate and the convective boiling mechanisms to the heat transfer coefficient can either be added linearly [20] or asymptotically [44] according to Eqs. (22) and (23), respectively:

$$h_{\mathrm{tp}} = h_{\mathrm{nb}} + h_{\mathrm{cv}}, \tag{22}$$

$$h_{\mathrm{tp}} = \left((h_{\mathrm{nb}})^n + (h_{\mathrm{cv}})^n\right)^{1/n}. \tag{23}$$

In the current study, a Chen-type correlation was used to predict the two-phase heat transfer coefficient. According to Chen [20], for in-tube forced convective boiling:

$$h_{\mathrm{tp}} = Fh_{\mathrm{sp}} + Sh_{\mathrm{nb}}, \tag{24}$$

where the enhancement factor, F, for in-tube systems is defined as:

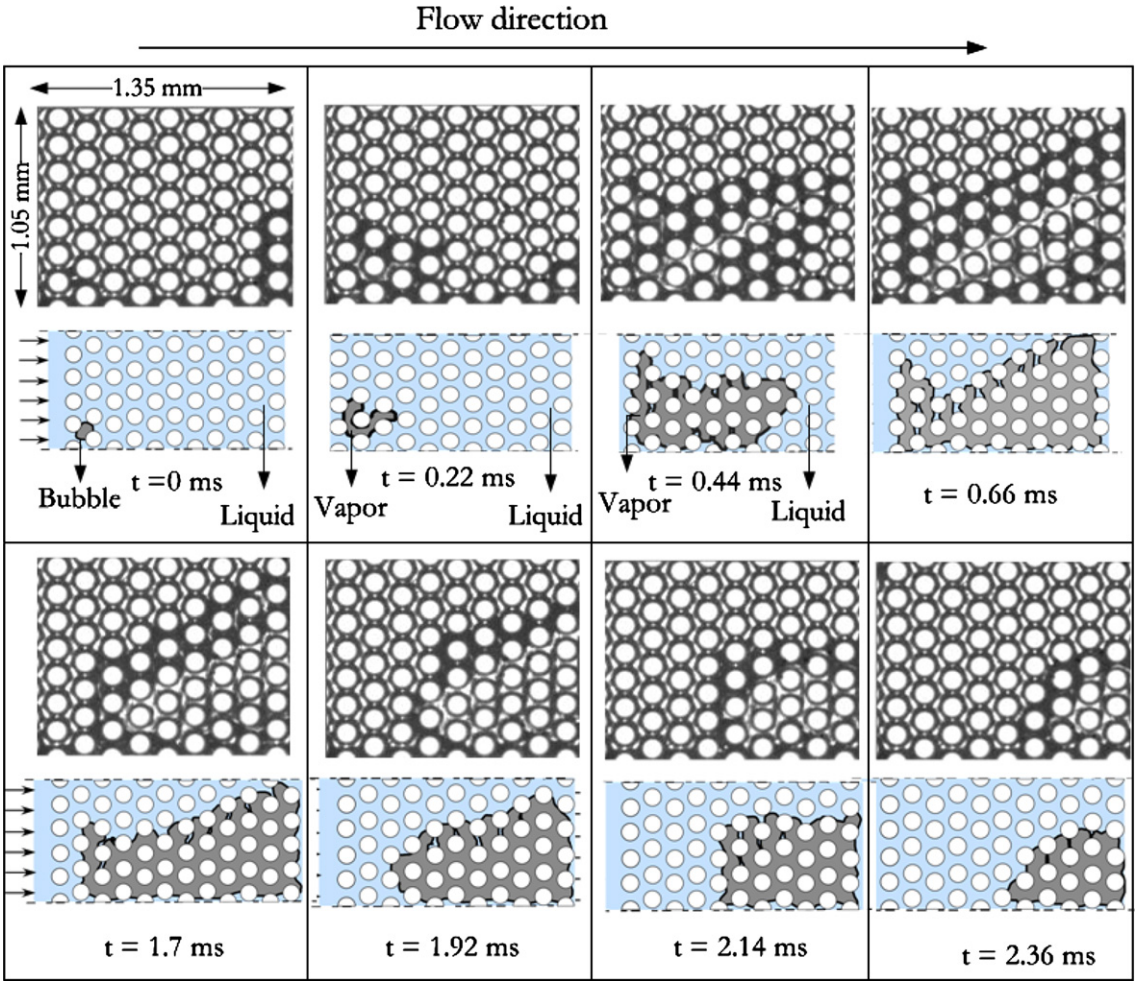

Fig. 10. Sequential images of nucleated bubble ($t = 0$) growing in size to form vapor slugs ($t = 1.7$–2.36 ms) and exiting the channel.

$$F = ((\phi_{L,tt})^2)^{0.89}, \tag{25}$$

and the suppression factor, S:

$$S = 0.9622 - 0.5822\left[\tan^{-1}\left(\frac{Re_f F^{1.25}}{6.81 \times 10^4}\right)\right]. \tag{26}$$

The correlation in the above form cannot be directly applied to the current study for two reasons. First, it was developed for turbulent flow, while the flow for both phases in the current study was laminar. Second, scaling laws require the model and the prototype to be geometrically similar. Nevertheless, an adaptation of Chen's correlation for crossflow over tube bundles was successfully developed by Jensen and Hsu [21] and Hwang and Yao [22].

Since the flow patterns analysis and the two-phase heat transfer coefficient results indicate that convective boiling is the dominant heat transfer mechansim, the contribution of the nucleate boiling term in Eq. (24) is neglected. Eq. (24) thus, reduces to:

$$h_{tp} = Fh_{sp}. \tag{27}$$

The enhancement factor will now be derived similar to Chen [20] and Bennet et al. [19]. But first, an appropriate single-phase Nusselt number needs to be selected. It has been recently shown that the Nusselt number in configuration similar to the present one has different Reynolds number functionality for $Re < 100$ than for $Re > 100$ [12]. Since Koşar and Peles's [11] Nusselt number correlation is valid for $Re < 100$ and the two-phase Reynolds number of the current study is higher, Short et al. [45] correlation is used for the single-phase heat transfer coefficient:

$$Nu = 0.76\left(\frac{S_t}{d}\right)^{0.16}\left(\frac{S_l}{d}\right)^{0.2}\left(\frac{L}{d}\right)^{-0.11} Re^{0.33} \tag{28}$$

Using the above equation, the two-phase heat transfer coefficient, h_{tp}, is thus, written:

$$h_{tp} = 0.76\left(\frac{S_t}{d}\right)^{0.16}\left(\frac{S_l}{d}\right)^{0.2}\left(\frac{L}{d}\right)^{-0.11} Re_{tp}^{0.33}\left(\frac{k_{f,tp}}{d}\right), \tag{29}$$

where $Re_{d,tp} = \frac{dv_{tp}\rho_f}{\mu_f}$ is the two-phase Reynolds number. Substituting Eqs. (21) and (29) into Eq. (27), the enhancement factor is written as:

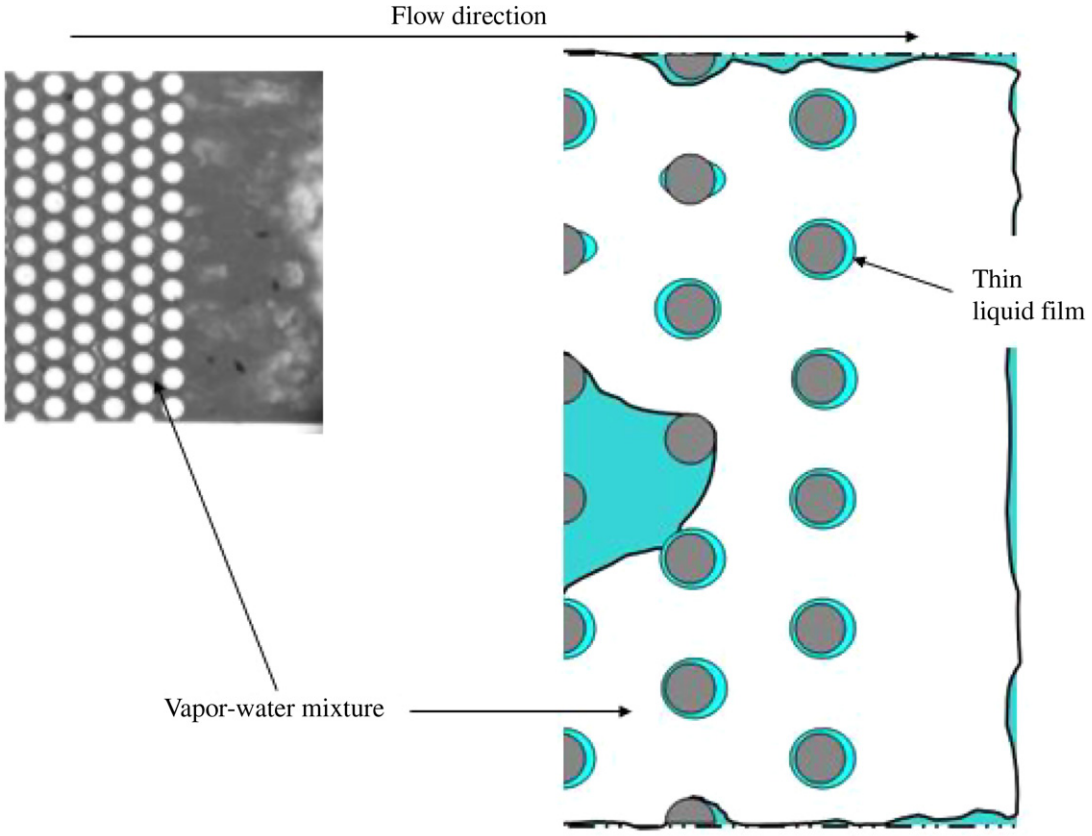

Fig. 11. Video image and schematic of the annular flow pattern.

$$F = \frac{h_{tp}}{h_s} = \left(\frac{Re_{d,tp}}{Re_{d,f}}\right)^{0.33}\left(\frac{k_{tp}}{k_f}\right). \tag{30}$$

While Reynolds analogy can not be fully justified when flow separation occurs, it has been argued that the analogy can still be used with reasonable agreement in crossflow over tube bundles [21,22]. Applying the Reynolds analogy:

$$\frac{-k_{tp}\frac{dT}{dy}}{q''_w(0)} = \frac{\mu_{tp}\frac{du}{dy}}{\tau_w(0)}, \tag{31}$$

or:

$$-\frac{k_{tp}}{\mu_{tp}}\,dT = \frac{q''_w(0)}{\tau_w(0)}\,du. \tag{32}$$

Assuming v_{tp} and T_b to be the velocity and the temperature of the bulk fluid respectively, and T_w to be the wall temperature, Eq. (32) can be integrated as:

$$\int_{u=0}^{v_{tp}} \frac{q''_w(0)}{\tau_{w,tp}}\,du = -\int_{T=T_w}^{T_b} \frac{k_{tp}}{\mu_{tp}}\,dT, \tag{33}$$

$$\frac{q''_w(0)}{\tau_{w,tp}}v_{tp} = \frac{k_{tp}}{\mu_{tp}}(T_w - T_b), \tag{34}$$

$$h_{tp} = \frac{q''_w(0)}{T_w - T_b} = \frac{\tau_{w,tp}(0)k_{tp}}{v_{tp}\mu_{tp}}. \tag{35}$$

Considering the liquid to flow alone through the channel at a velocity of V_f, a similar expression can be written as:

$$h_f = \frac{\tau_w(0)k_f}{v_f\mu_f}. \tag{36}$$

Assuming the thermophysical properties to be equal, the ratio of h_{tp}/h_f may be written as:

$$\frac{h_{tp}}{h_f} = \frac{\tau_{w,tp}}{\tau_{w,f}}\frac{v_f}{v_{tp}} = \frac{\tau_{w,tp}}{\tau_{w,f}}\frac{Re_{d,f}}{Re_{d,tp}}. \tag{37}$$

Shear stress terms in the above equation can also be expressed in terms of the two-phase frictional multiplier, $(\phi_l)^2$, which reduces Eq. (37) to:

$$\frac{h_{tp}}{h_f} = (\phi_l)^2\frac{Re_{d,f}}{Re_{d,tp}}. \tag{38}$$

Combining Eqs. (30) and (38), the ratio of $Re_{d,f}/Re_{d,tp}$ can be written as:

$$\frac{Re_{d,f}}{Re_{d,tp}} = (\phi_l^2)^{\frac{-1}{1.33}}. \tag{39}$$

Substituting Eq. (39) in Eq. (30),

$$F = (\phi_l^2)^{0.2475}. \tag{40}$$

The above equation is valid for liquids with $Pr \approx 1$. Following the method adopted by Bennett et al. [19], for $Pr \neq 1$, Eq. (40) is multiplied by $Pr^{0.333}$:

$$F = (\phi_l^2)^{0.2475}Pr^{0.333}. \tag{41}$$

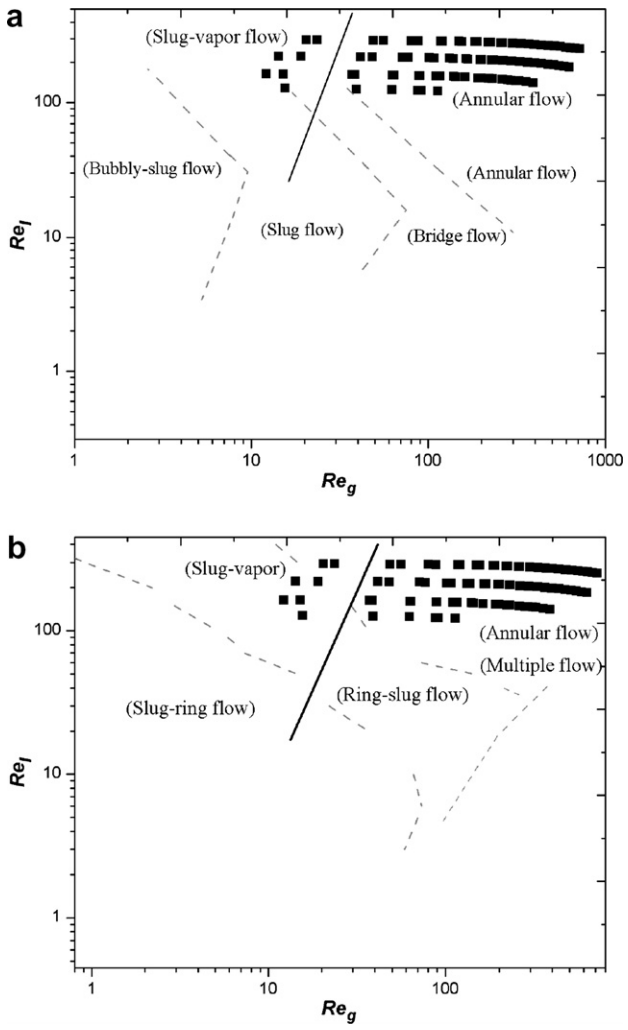

Fig. 12. Comparison of current flow map with: (a) Krishnaurthy and Peles [32], and (b) Kawahara et al. [29] adiabatic flow map.

Similar to the method followed by Zhang and Hibiki [46], an adjustment parameter, ζ, is also included. The final equation can be written as:

$$F = \zeta(\phi_l^2)^{0.2475} Pr^{0.333}, \tag{42}$$

and the two-phase heat transfer coefficient can be written as:

$$h_{tp} = \zeta(\phi_l^2)^{0.2475} Pr^{0.333} h_{sp}. \tag{43}$$

All the thermophysical properties in the above equations are calculated at the saturation temperature.

Correlations for frictional multiplier in micro-scale are very limited. Krishnamurthy and Peles [32] developed a correlation for a configuration similar to the current study but at lower liquid Reynolds numbers ($Re < 50$):

$$(\phi_l)^2 = 1 + \frac{C_1 Re_d}{X_{vv}} + \frac{1}{X_{vv}^2}, \tag{44}$$

where the constant $C_1 = 0.0358$ is an empirically defined constant. However, in the current study, under saturation conditions, the liquid Reynolds number ranged from 150 to 300. Thus, the correlation developed by Kawahara et al. (Eq. (19)) for micro-channel for higher Reynolds numbers (2–1000) is used in Eq. (43).

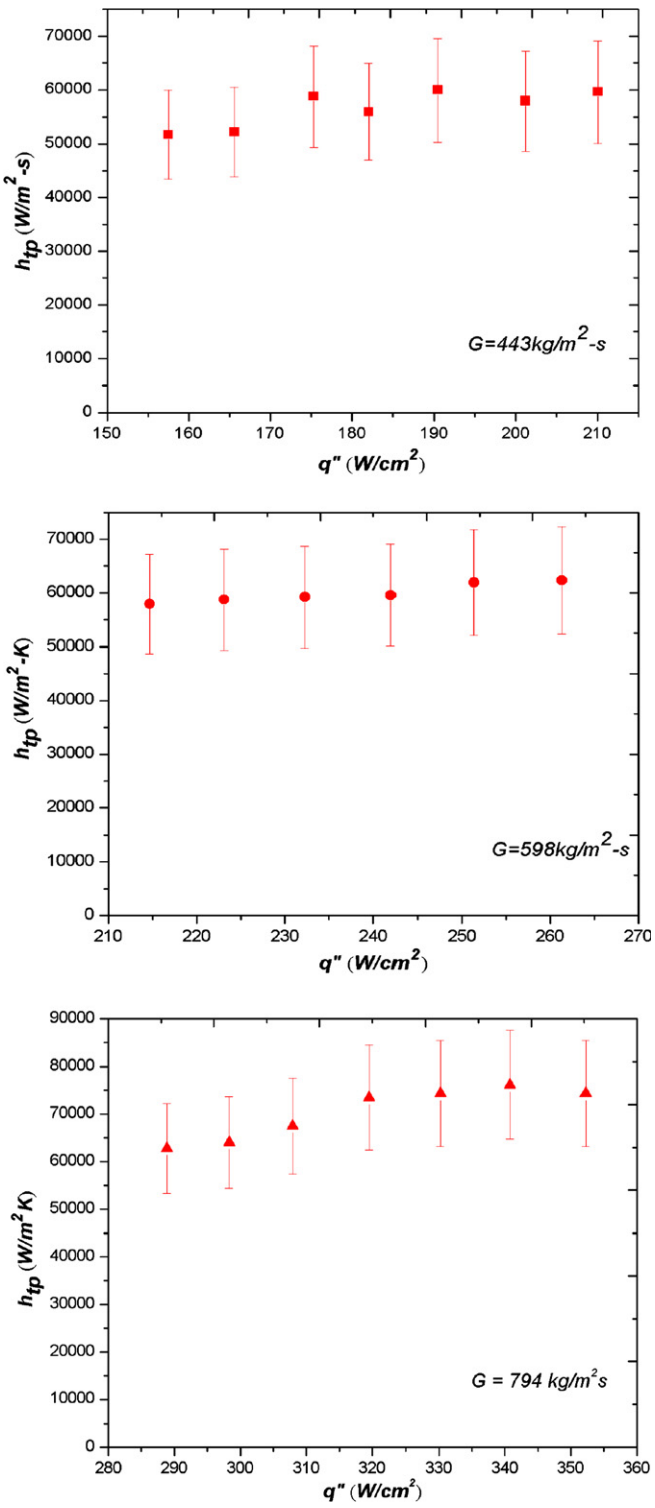

Fig. 13. Two-phase heat transfer coefficient for different mass fluxes.

$$(\phi_l)^2 = 1 + \frac{0.24}{X_{vv}} + \frac{1}{X_{vv}^2}, \tag{45}$$

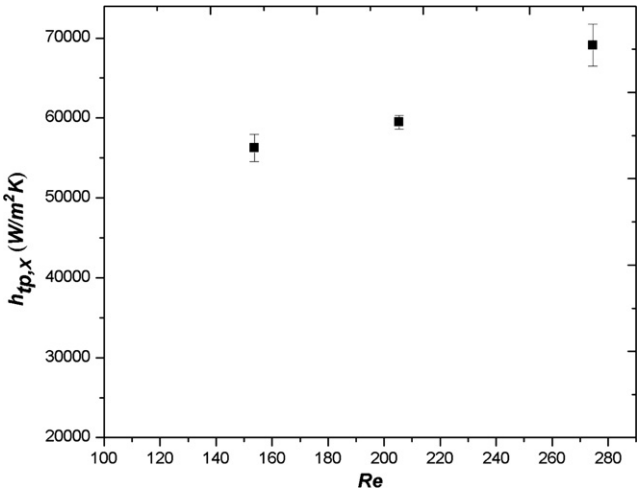

Fig. 14. The variation of local heat transfer coefficient as a function of mass flux.

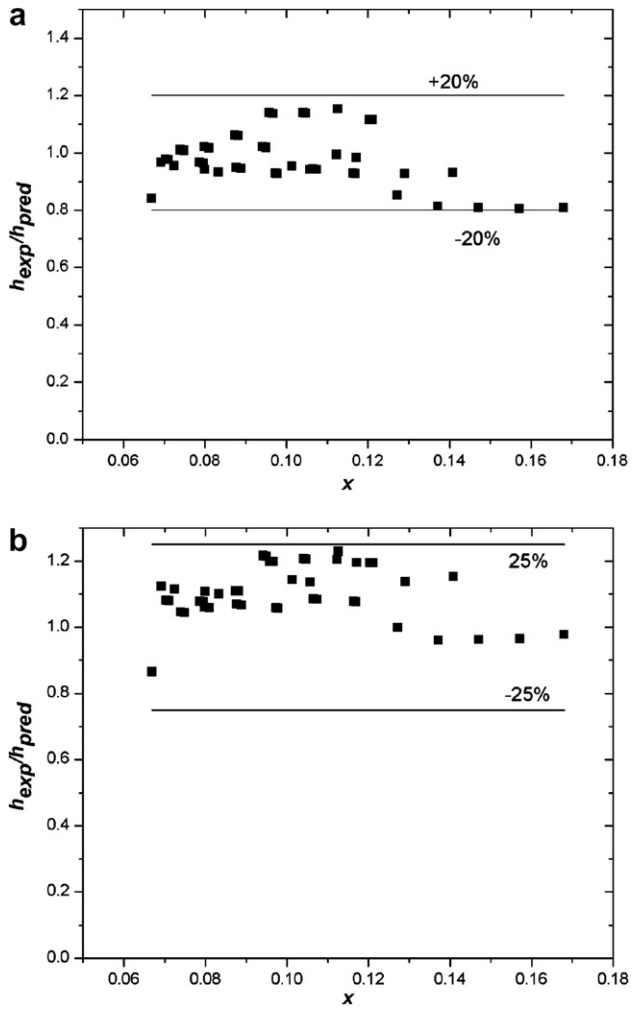

Fig. 15. Comparison of the experimental results with the correlation from: (a) Kawahara et al. [29], and (b) Krishnamurthy and Peles [32].

The value of the adjustment parameter, ζ, in Eq. (43) was obtained by using the least square method and was found to be 1.4 while using the micro-channel correlation for frictional multiplier. Fig. 15a shows the ratio of the predicted two-phase heat transfer coefficient and the experimental data as a function of exit quality using Kawahara et al. [29] correlation for frictional multiplier. All the data fall within $\pm 20\%$ of the experimental results. But using the adjustable parameter to obtain the agreement between the experimental and predicted results indicates that Kawahara's et al. [29] correlation under-predicts the two-phase heat transfer coefficient. The discrepancy between the predicted and experimental values can be attributed to different flow configurations for which the frictional multiplier correlation has been developed. Unlike plain micro-channels, channel with pin fins have enhanced heat transfer due to increased convective mixing and increased surface area. As a result the hydrodynamic characteristics of the flow is not completely captured by the use of a correlation developed for micro-channel. Thus, there is a need to use a correlation that is specific to the current flow configuration. The frictional multiplier correlation developed by Krishnamurthy and Peles [32], though valid for low Reynolds number, can be used in Eq. (43) because it was developed for similar flow configuration. Fig. 15b shows that the resulting correlation is able to predict the experimental results within $\pm 25\%$ with the value of adjustment parameter, ζ, equal to unity. This demonstrates that the frictional multiplier correlation specific to the flow configuration results in better agreement with the experimental results. The discrepancy in the agreement of the experimental results and predicted heat transfer coefficients while using the Krishnamurthy and Peles correlation [32] can be reduced by developing a correlation for frictional multiplier that is valid for a wider range of Reynolds number.

5. Conclusions

In this study, flow boiling of water across a bank of circular staggered micro-pin fins was investigated. Local temperature measurements were used to obtain local single-phase and two-phase heat transfer coefficients. Single-phase heat transfer coefficients were compared with micro-scale correlation for similar flow configuration and good agreement was obtained. The main conclusions from this study are stated below:

(1) Two-phase heat transfer coefficient was observed to be moderately dependent on the mass flux and independent of the heat flux.
(2) Flow patterns were observed through flow visualization and classified as vapor slug and annular flow.
(3) The observed flow patterns were mapped as a function of superficial gas (Re_g) and liquid (Re_l) Reynolds numbers to construct a flow map, which was compared with flow maps from other micro-scale studies. Good agreement with respect to the flow patterns was observed.
(4) Based on the observed dominant flow patterns (annular flow) and the characteristic of the two-phase heat

transfer coefficient, the heat transfer mechanism was determined to be convective boiling.

(5) A superposition model for predicting the two-phase heat transfer coefficient in convective boiling was developed based on Reynolds analogy. The semi-empirical model showed reasonable agreement with experiments.

(6) The discrepancy in the predicted values can be attributed to a lack of sufficient correlations for two-phase frictional multiplier at the micro-scale.

Acknowledgements

This work was supported by the Office of Naval Research. The micro-fabrication was performed in part at the Cornell NanoScale Facility (a member of the National Nanotechnology Infrastructure Network) which is supported by the National Science Foundation under Grant ECS-0335765, its users, Cornell University and industrial affiliates.

References

[1] G. Celata, M. Cumo, G. Zummo, Thermal-hydraulic characteristics of single-phase flow in capillary pipes, Exp. Therm. Fluid Sci. 28 (2–3) (2004) 87.

[2] S. Kandlikar, W. Grande, Evaluation of single-phase flow in microchannels for high heat flux chip cooling-thermohydraulic performance enhancement and fabrication technology, J. Heat Transfer 25 (8) (2004) 5.

[3] W. Owhaib, B. Palm, Experimental investigation of single-phase convective heat transfer in circular microchannels, Exp. Therm. Fluid Sci. 28 (2–3) (2004) 105–110.

[4] J. Li, G. Peterson, P. Cheng, Three-dimensional analysis of heat transfer in a micro-heat sink with single-phase flow, Int. J. Heat Mass Transfer 47 (2004) 4215.

[5] P. Lee, S. Garimella, Investigation of heat transfer in rectangular microchannels, Int. J. Heat Mass Transfer 48 (2005) 1688.

[6] A. Koşar, C.-J. Kuo, Y. Peles, Reduced pressure boiling heat transfer in rectangular microchannels with interconnected reentrant cavities, J. Heat Transfer 127 (10) (2005) 1106.

[7] A. Koşar, C.J. Kuo, Y. Peles, Boiling heat transfer in rectangular microchannels with reentrant cavities, Int. J. Heat Mass Transfer 48 (2005) 4867.

[8] S.G. Kandlikar, Two-phase flow patterns, pressure drop, and heat transfer during boiling in minichannels flow passages of compact evaporators, Heat Transfer Eng. 23 (1) (2002) 5.

[9] W. Qu, I. Mudawar, Flow boiling heat transfer in two-phase microchannel heat sink: Part 1. Experimental investigation and assessment of correlation methods, Int. J. Heat Mass Transfer 46 (15) (2003) 2755.

[10] A. Koşar, Y. Peles, Thermal-hydraluic performance of MEMS based pin fin heat sink, J. Heat Transfer 128 (2006) 121.

[11] A. Koşar, Y. Peles, Convective flow of refrigerant (R-123) across a bank of micro pin fins, Int. J. Heat Mass Transfer 49 (2006) 3142.

[12] R. Prasher, J. Dirner, J.-Y. Chang, A. Myers, D. Chau, D. He, S. Prstic, Nusselt number and friction factor of staggered arrays of low aspect ratio micropin-fins under cross flow for water as fluid, J. Heat Transfer 129 (2) (2007) 141.

[13] A.M. Siu-Ho, W. Qu, F. Pfefferkorn, Pressure drop and heat transfer in a single-phase micro-pin-fin heat sink, in: ASME International Mechanical Engineering Congress and Exposition, November 5–10 IMECE2006-14777.

[14] E. Colgan, B. Furman, M. Gaynes, W. Graham, N. LaBianca, J. Magerlein, R. Polastre, M. Rothwell, R. Bezama, R. Choudhary, K. Marston, H. Toy, J. Wakil, J. Zitz, R. Schmidt, A practical implementation of silicon microchannel coolers for high power chips, IEEE Trans. Compon. Pack. Technol. 30 (2) (2007) 218–225.

[15] D. Chisholm, A.D.K. Laird, Two-phase flow in rough tubes, Trans. ASME 80 (1949) 276.

[16] R. Dowlati, M. Kawaji, A.M.C. Chan, Void fraction and friction pressure drop in two-phase flow across a horizontal tube bundle, AICHE Sympos. Ser. 184 (1988) 126.

[17] R. Dowlati, A.M.C. Chan, M. Kawaji, Hydrodynamics of two-phase flow across horizontal in-line and staggered rod bundle, J. Fluids Eng. 114 (1992) 450.

[18] D.S. Schrage, J.-T. Hsu, M.K. Jensen, Two-phase pressure drop in vertical cross-flow across a horizontal tube bundle, AICHE J. 34 (1988) 107.

[19] L. Bennett, J. Chen, Forced convective boiling in vertical tubes for saturated components and binary mixtures, J. Am. Inst. Chem. Eng. 26 (1980) 454.

[20] J.C. Chen, Correlation for boiling heat transfer to saturated fluids in convective flow, I and EC Process Design Develop. 5 (3) (1966) 322.

[21] M.K. Jensen, J.-T. Hsu, A parametric study of boiling heat transfer in horizontal tube bundle, Trans. ASME 110 (1988) 976.

[22] T.H. Hwang, S.C. Yao, Forced convective boiling in horizontal tube bundles, Int. J. Heat Mass Transfer 29 (5) (1986) 785.

[23] G.T. Polley, T. Ralston, I.D.R. Grant, Forced crossflow boiling in an ideal in-line tube bundle, ASME 80-HT-46.

[24] I.D.R. Grant, D. Chislom, Two-phase flow on the shell-side of a segmentally baffled shell-and-tube heat exchanger, Trans. ASME 101 (1979) 38.

[25] R. Dowlati, M. Kawaji, A.M.C. Chan, Two-phase crossflow and boiling heat transfer in horizontal tube bundles, Trans. ASME 118 (1996) 124.

[26] P.M.-Y. Chung, M. Kawaji, The effect of channel diameter on adiabatic two-phase flow characteristics in microchannels, Int. J. Multiphas. Flow 30 (2004) 735.

[27] T. Cubaud, C.-M. Ho, Transport of bubbles in square microchannels, Phys. Fluids 16 (2004) 4575.

[28] M. Kawaji, P.M.Y. Chung, Adiabatic gas-liquid flow in microchannels, Microscale Thermophys. Eng. 8 (2004) 239.

[29] A. Kawahara, P.M.-Y. Chung, M. Kawaji, Investigation of two-phase flow pattern, void fraction and pressure drop in a microchannel, Int. J. Multiphas. Flow 28 (2002) 1411.

[30] S. Garimella, V. Singhal, Single-phase flow and heat transport and pumping considerations in microchannel heat sinks, Heat Transfer Eng. 25 (1) (2004) 15.

[31] A. Koşar, Y. Peles, Boiling heat transfer in a hydrofoil-based micro pin fin heat sink, Int. J. Heat Mass Transfer 50 (5–6) (2007) 1018.

[32] S. Krishnamurthy, Y. Peles, Gas-liquid two-phase flow across a bank of micro pillars, Phys. Fluids 19 (4) (2007) 043302.

[33] C.-J. Kuo, A. Koşar, Y. Peles, S. Virost, C. Mishra, M. Jensen, Bubble dynamics during boiling in enhanced surface microchannels, J. Microelectromech. Syst. 15 (6) (2006) 1514.

[34] P.C. Lee, F.G. Tseng, C. Pan, Bubble dynamics in micro channels. Part I: Single microchannel, Int. J. Heat Mass Transfer 47 (2004) 5575.

[35] S. Kandlikar, P. Balasubramanian, Effect of gravitational orientation on flow boiling of water in 1054 × 197 micron parallel minichannels, J. Heat Transfer 127 (2005) 820.

[36] J.R. Thome, Boiling in microchannels: a review of experiment and theory, Int. J. Heat Fluid Flow 24 (2004) 128–139.

[37] V. Dupont, J. Thome, Evaporation in microchannels: influence of the channel diameter on heat transfer, Microfluidics Nanofluidics 1 (2) (2005) 119.

[38] H. Lee, S. Lee, Pressure drop correlations for two-phase flow within horizontal rectangular channels with small heights, Int. J. Multiphas. Flow 27 (2001) 783.

[39] K. Mishima, T. Hibiki, Some characteristics of air–water two-phase flow in small diameter vertical tubes, Int. J. Multiphas. Flow 22 (1996) 703.
[40] R. Dowlati, M. Kawaji, A.M.C. Chan, Pitch-to-diameter effect on two-phase flow across an in-line tube bundle, AICHE J. 36 (1990) 765.
[41] A. Koşar, C.-J. Kuo, Y. Peles, Suppression of boiling flow oscillations in parallel microchannels with inlet restrictors, J. Heat Transfer 128 (3) (2006) 251.
[42] V.P. Carey, Liquid–Vapor Phase-Change Phenomena, Taylor & Francis, 1992.
[43] A.B. Cohen, E. Rahim, Modeling and prediction of two-phase refrigerant flow regimes and heat transfer characteristics in micro-gap channels, in: Proceedings of ASME ICNMM, June 18–20, 2007.
[44] R.L. Webb, N.S. Gupte, A critical review of correlations for convective vaporization in tubes and tube banks, Heat Transfer Eng. 13 (3) (1992) 58.
[45] B.E. Short, P.E. Raad, D.C. Price, Performance of pin fin cast aluminum, coldwalls, Part 2: Colburn j-factor correlations, J. Thermophys. Heat Transfer 16 (2002) 397–403.
[46] W. Zhang, T. Hibiki, K. Mishima, Correlation for flow boiling heat transfer at low liquid reynolds number in small diameter channels, J. Heat Transfer 127 (2005) 1214.